Journal of Energy Chemistry 122 (2026) 223–234

Contents lists available at ScienceDirect

Journal of Energy Chemistry

journal homepage: www.elsevier.com/locate/jechem

http://www.journals.elsevier.com/journal-of-energy-chemistry/

Unveiling structural evolution and performance of hybrid-functional catalyst in plastic pyrolysis–catalytic gasification process

Tian Heng Qin [a], Oxana V. Magdysyuk [b], Shaoliang Guan [c], Zhuze Shao [d], Tian Wang [a], Shogo Kumagai [d,e], Toshiaki Yoshioka [d], Boyu Qu [f], Guozhao Ji [f], Davide Dionisi [a], Jos Derksen [a], Ye Shui Zhang [a,*]

[a] School of Engineering, University of Aberdeen, Aberdeen AB24 3UE, UK
[b] EaStCHEM, University of St Andrews, St Andrews KY16 9ST, UK
[c] Maxwell Centre, Cavendish Laboratory, University of Cambridge, Cambridge CB3 0HE, UK
[d] Graduate School of Environmental Studies, Tohoku University, Sendai 980-8579, Miyagi, Japan
[e] Graduate School of Engineering, Tohoku University, Sendai 980-8579, Miyagi, Japan
[f] Key Laboratory of Industrial Ecology and Environmental Engineering, School of Environmental Science & Technology, Dalian University of Technology, Dalian 116024, Liaoning, China

ARTICLE INFO

Article history:
Received 1 May 2026
Revised 4 July 2026
Accepted 12 July 2026
Available online 23 July 2026

Keywords:
Pyrolysis–catalytic gasification
Hydrogen
Hybrid-functional catalyst
Plastic waste
In situ PXRD

ABSTRACT

Conventional metal-loaded zeolite catalysts often suffer from deactivation due to coking and sintering. To address this, hybrid-functional Ni-CaO-Ca_2SiO_4 catalyst was prepared and evaluated for H_2-rich syngas production by pyrolysis–catalytic gasification process, achieving maximum H_2 yield of 113.21 mmol g^{-1} $_{of\ plastic}$. The catalyst deactivation behavior, along with the structural evolution and surface chemistry of the hybrid-functional catalyst, was investigated by means of both ex situ and in situ characterization techniques. After cycles, Ni oxidation at the surface of particle, slight Ni sintering, a decrease in Ni/NiO ratio, and surface enrichment of O–C=O species were observed. Although metallic Ni was detected by PXRD (Powder X-ray diffraction) in the bulk, surface X-ray photoelectron spectroscopy (XPS) revealed the absence of metallic Ni and the predominance of NiO on the catalyst surface, suggesting surface-initiated deactivation and pore blockage. In situ PXRD results confirmed the reduction of NiO by pyrolysis products. These findings elucidate the fundamental behavior of the catalyst under realistic conditions and provide practical insights for designing durable and efficient catalysts for waste valorization. These dynamic observations distinguish this work from studies based mainly on post-reaction characterization and provide mechanistic insight into catalyst activation, deactivation, and structural evolution. The integrated ex situ/in situ approach offers a useful framework for designing durable catalysts for plastic-waste valorisation.

1. Introduction

Although personal protective equipment, such as plastic masks, has gradually faded from public memory following the pandemic, global plastic production increased from 400.4 Mt in 2022 to 413.8 Mt in 2023 [1,2]. Meanwhile, only 0.1% of global plastic waste underwent chemical recycling, while less than 0.1% was captured as carbon. Given the escalating environmental concerns, it is essential to enhance current plastic waste management methods to meet rising demands and challenge. Global H_2 production reached 97 Mt in 2023 and remained largely dependent on unabated fossil fuels [3]. However, low-carbon H_2 which relies mostly on production from fossil fuels integrated with carbon capture, utilisation and storage (CCUS) technologies accounts for less than 1% of global production. Based on announced projects, low-carbon H_2 production could reach 49 Mt per annum by 2030 [4], underscoring the accelerating global commitment to clean H_2 technologies. H_2 production techniques such as photocatalysis [5,6], electrocatalysis [7,8], plasma catalysis [9,10], mechanocatalysis [11], dry reforming [12,13] and others [14,15] have been widely reported. Pyrolysis–catalytic gasification with the designed hybrid-functional catalyst is a relatively mature CCUS-aligned technology, wherein plastics decompose to radicals intermediates that are subsequently catalytically gasified in steam to yield H_2-rich syngas, offering both sustainable H_2 production and plastic waste mitigation [16–18]. Typically, pyrolysis–catalytic

* Corresponding author.
E-mail address: yeshui.zhang@abdn.ac.uk (Y.S. Zhang).

https://doi.org/10.1016/j.jechem.2026.07.030

gasification catalysts consist of active metals supported on mesoporous molecular sieves, especially zeolites with silica/alumina frameworks [19–21]. These catalysts continue to be extensively employed and exhibit remarkable resilience and adaptability, finding wide application in H_2 production [22], liquid hydrocarbon production [23], carbon nanotube synthesis [24], hydroconversion of plastic oils [25] and even in the dry reforming of methane [26]. However, these conventional catalysts are prone to rapid deactivation, primarily due to coking, metal sintering, encapsulation, poisoning, and degradation of the catalyst support framework [27–29]. In response, recent studies have explored various modifications to both the active metals and the catalyst supports, including the incorporation of bimetallic systems, lowering the operating temperature to reduce energy consumption [15,30], carbon dioxide (CO_2) sorbents as well as structural stabilisers [12,16,31–34]. These efforts are largely motivated by the complexity of radical species generated during the high-temperature pyrolysis of plastics. For instance, hydrolysis and pyrolysis can occur simultaneously during the steam reforming of polyesters [35], which subsequently undergo catalytic gasification to yield H_2 and unwelcomed carbon deposition. While some efforts have been made to elucidate the underlying mechanisms, detailed understanding of the dynamic structural evolution of catalysts during this two-step process remains limited. This research gap continues to hinder the development of more efficient and durable catalytic systems.

Building on this context, Ni-CaO-Ca_2SiO_4 catalysts were employed to unveil the structural evolution and catalytic performance during pyrolysis–catalytic gasification of plastic for H_2-rich syngas production. Compared with conventional Ni-supported molecular sieves, the structural transformations during and after reaction can be more clearly characterised, offering deeper insight into structure–performance relationships. In previous work, we have proved that Ni loading is the decisive factor for enhancing H_2 and syngas production irrespective of the samples porous properties [16]. Moreover, Ca_2SiO_4 plays a significant role in suppressing catalyst sintering and formation of favourable active metal distribution [16]. Nickel was selected for its proven ability to cleave C–C and C–O bonds [36–38]. CaO, serving as both a major structural component and a CO_2 sorbent, promotes reaction equilibrium and suppresses coking [28,39–41]. Ca_2SiO_4 acts as a structural stabilizer, forming sintering-resistant and anti-agglomeration sea anemone-like morphologies [12,16,32]. Representative studies on H_2 production from solid-waste pyrolysis–catalytic gasification are summarised in Table 1. These studies support the rationale for using CaO-containing catalyst systems and indicate the broader relevance of this design strategy for solid waste conversion.

In recent years, research on H_2 production via solid waste pyrolysis–catalytic gasification has primarily focused on improving catalyst design [32,42], employing cost-effective catalysts [43], reducing the reaction temperature [44], and exploring alternative catalytic approaches such as microwave-assisted catalysis [47]. Although the deactivation of conventional metal–zeolite catalysts under high-temperature conditions is well documented, the extent and underlying mechanisms of deactivation under specific experimental conditions remain insufficiently investigated.

The effects of real-world plastic feedstock type, gas collection time, water injection rate, and cyclic stability on H_2-rich syngas production were investigated, which was as high as 113.21 mmol g^{-1} $_{of\ plastic}$. A combination of ex situ techniques, including thermogravimetric analysis (TGA), scanning electron microscopy (SEM), energy-dispersive X-ray spectroscopy (EDS), high-angle annular dark-field scanning transmission electron microscopy (HAADF-STEM), PXRD, XPS, and pyrolysis gas chromatography–mass spectrometry (Py-GC–MS), along with in situ PXRD, was employed to monitor the structural evolution of pre- and post-reaction catalysts. Particular attention was given to carbon deposition and the evolution of Ni and NiO, including the crystallite size, molar ratio, surface atomic concentration and unit cell volume. These findings offer insights into deactivation mechanisms and inform future design of hybrid-functional catalysts.

2. Experimental

2.1. Materials

All chemicals used in this research were purchased from Sigma-Aldrich, UK with purities over 99%. The preparation of the catalyst has been reported previously. 5 mmol of tetraethyl orthosilicate (TEOS, $Si(OC_2H_5)_4$) was dissolved in 500 mL of 1 mmol L^{-1} nitric acid (HNO_3) and stirred at 600 r min^{-1} at room temperature (RT) for 45 min. Then, 45 mmol calcium acetate hydrate ($Ca(C_2H_3O_2)_2$) and 3.4980 g of nickel(II) nitrate hexahydrate ($Ni(NO_3)_2{\cdot}6H_2O$) were added to the solution after TEOS was completely hydrolyzed. After the precursor became homogeneous, it was dried at 95 °C in an oven overnight. All the dried precursors were calcined at 850 °C (ramping rate 5 °C min^{-1}) for 1 h in air. The catalyst sample was denoted as Ni-CaO-Ca_2SiO_4 and sieved to a size between 50 to 180 μm before experiments and characterization. Volvic natural mineral water (500 mL) bottles, caps, and

Table 1
Comparison of catalytic performance and reaction configurations for H_2 production from waste solid pyrolysis–catalytic gasification.

Catalyst	Feedstock	Reaction temperature	Reaction configuration	Highest H_2 yield & selectivity	References
Ni-CaO-Ca_2SiO_4	Plastics	900 °C	Two-stage fix-bed reactor, gasification	113.21 mmol g^{-1} $_{of\ LDPE}$ and 58.1 mmol g^{-1} $_{of\ PET}$ 63.53 vol%	This work
Ni-CaO-Ca_2SiO_4	Sawdust	850 °C	Mixed feed in TG-MS	626 mL H_2 g^{-1} $_{of\ sawdust}$, ~61 vol%	[32]
Li_2CO_3-Na_2CO_3-K_2CO_3 molten salt	Corn cob	600–900 °C	Feedstock inlet with CaO and steam	832.90 mL H_2 g^{-1} $_{of\ biomass}$, 68.67 vol%	[42]
CaO (SS)–LR (leaching residue from steel slag)	Chinese medicine residues	600–800 °C	Steam reforming	15.13 mmol g^{-1} $_{of\ feedstock}$, 67.5 vol%	[43]
$La_{10}Al_{10}$-Ni_5/CaO	Cellulose	450–500 °C	Two-stage fix-bed reactor, gasification, mild operating conditions	26.5 mmol g^{-1} $_{of\ cellulose}$, 98.8% purity	[44]
CaO	Cellulose	550–800 °C	Two-stage fix-bed reactor, gasification	680 mL H_2 g^{-1} $_{of\ cellulose}$, ~ 50 vol%	[45]
CaO	Plastic, woody biomass	650–950 °C	Simulation using Aspen Plus	65.2 mol%	[46]

Reported values follow the yield basis used in the original publications.

labels were cut into small fragments (15 × 3 mm) as feedstock and denoted as PET, HDPE (high-density polyethylene) and LDPE (low-density polyethylene) respectively. The proximate and ultimate analyses of those feedstocks were obtained from SOCOTEC, UK and given in Table S1.

2.2. Experimental set-up

Experiments were undertaken using a two-stage fixed-bed reactor for pyrolysis–catalytic gasification experiments (Fig. S1) [16]. Pyrolysis of the plastic waste occurred in the first stage at 600 °C, and the produced volatiles were passed directly to the second stage, where catalytic reactions occurred at 900 °C. Nitrogen (N_2) was introduced into the process from the top of the pyrolysis reactor as the inert purge gas with a flow rate of 110 mL min^{-1}. The plastic sample (0.5 g) was placed in the first stage, and the catalyst (0.5 g) was placed in the bottom stage; quartz wool (around 0.5 g) was used to spread out the catalyst. During the experiments, the catalyst bed (second stage) was preheated to 900 °C. Then, the pyrolysis stage was heated from RT to 600 °C with a heating rate of 40 °C min^{-1}. Water was introduced into the second stage of the process via a syringe pump with a flow rate of 1.5, 3.75, and 5 mL h^{-1}, respectively. Heating of the top pyrolysis stage, water injection and gas collection started at the same time. The gaseous products from the process were passed to a condensation system to trap the condensable liquids, followed by gas collection in a 12 L Tedlar® gas sampling bag. The gas collection time was 60, 90, and 120 min respectively as one of the process optimization parameters.

2.3. Analytical methods

The gaseous products were collected by the Tedlar® gas sampling bag and analyzed by gas chromatography (GC) with a Thermal conductivity detector (TCD) using a capillary column (30 m × 0.25 mm, Thermo Scientific TraceGOLDTM TG-WaxMS A).

The spent catalysts were analyzed by temperature programmed oxidation (TPO) using a thermogravimetric analyzer (TGA) (Mettler Toledo TGA/DSC 3 + system) to determine the oxidation characteristics of carbon deposited on the catalyst. Each spent catalyst sample was placed in the TGA and heated in air at a flow rate of 20 mL min^{-1} to 900 °C at a heating rate of 15 °C min^{-1}. All the samples were held for 10 min at 120 °C to remove the moisture.

The spent catalysts were characterized by scanning electron microscopy (SEM) (Zeiss GeminiSEM 300) to determine surface morphologies of the catalyst particles. The element distributions of fresh catalysts were explored with energy-dispersive X-ray spectroscopy (EDS) associated with the SEM. High-angle annular dark field (HAADF) STEM (scanning transmission electron microscopy) and corresponding EDS imaging was performed with an FEI Titan Themis instrument.

X-ray photoelectron spectroscopy (XPS) Analysis was performed using a Thermo NEXSA G2 XPS fitted with a monochromated Al K_α X-ray source (1486.7 eV), a spherical sector analyzer and 3 multichannel resistive plate, 128 channel delay line detectors. All data was recorded at 19.2 W and an X-ray beam size of 400 × 200 μm. Survey scans were recorded at a pass energy of 200 eV, and high-resolution scans were recorded at a pass energy of 50 eV. Electronic charge neutralization was achieved using an ion source (Thermo Scientific FG-03). Ion gun current = 150 μA. Ion gun voltage = 40 V. All sample data was recorded at a pressure below 10^{-8} Torr and a room temperature of 294 K. Data was analysed using CasaXPS v2.3.26rev1.0 N. Peaks were fit with a Shirley background prior to component analysis. Line shapes of LA (1.53,243) were used to fit components.

Room temperature ex situ XRD data sets were obtained using a STOE Stadi-Powder X-ray diffractometer equipped with a Mo tube set to 55 kV and 40 mA ($K_\alpha 1$ with λ = 0.7093 Å), a primary beam monochromator and Dectris Mythen detector. Measurements was performed in this capillary (0.5 mm) transmission mode with the 2θ range of 2° to 50°. The data werre acquired using the STOE WinXPOW program (version 3.20). Rietveld refinement [48,49] of the solid solutions were performed using the Topas Academic 7.25 program [50].

For the in situ XRD analysis, the high-temperature reaction furnace HT2 (STOE) was used. Samples were loaded into the middle of thick quartz capillary tube with total length 160 mm, OD = 2 mm, ID = 1 mm. Sample of catalysts was positioned in the center of the quartz capillary tube with HDPE or PET powder placed on one side. The nitrogen gas was used as a carrier; the nitrogen flow was adjusted to approx. 30 mm^3 min^{-1}, which is very close to static nitrogen gas atmosphere. Accordingly, the capillary-based in situ PXRD experiment was used to monitor the relative sequence and tendency of phase transformations.

Pyrolysis of PET with Ni-CaO-Ca_2SiO_4 catalyst was conducted with a TR-GC/MS system composed of two μ-reactors (Rx-3050TR, Frontier Laboratories Ltd., Japan) interfaced with a high-pressure flow controller (HP-3050FC, Frontier Laboratories ltd., Japan) and a GC–MS (7890/5977B, Agilent Technologies, USA). An Ultra Alloy® Capillary Column UA^+-5 (30 m length, 0.25 mm i.d., 0.25 μm film thickness with 95% polydimethylsiloxane and 5% poly diphenyl dimethyl siloxane stationary phase, Frontier Laboratories Ltd., Japan) was used, with helium used as the carrier gas at a flow rate of 1 mL min^{-1}. After the catalytic stage reached 900 °C, the pyrolyzer was heated from RT to 600 °C at a rate of 20 °C min^{-1}. The pyrolysis products were trapped by a liquid nitrogen cryotrap before transferred to the MS through the separation column. The separated compounds were identified using MS (MS ion source/quadrupole temperature: 230/150 °C, acquisition mode: scan mode (4.83 s^{-1}), scan range: m/z 15–600) with high matching indices with respect to the NIST 08th and F-Search pyrolysis library databases.

3. Results and discussion

3.1. Catalytic performance testing

In this study, pyrolysis–catalytic gasification of plastic waste was conducted with a hybrid-functional Ni-CaO-Ca_2SiO_4 catalyst in a two-stage fixed-bed reactor. The optimum conditions, based on our previous research, were applied with an N_2 flow rate of 110 mL min^{-1}, a gas collection time of 1 h, and a catalytic temperature of 900 °C [16]. Four parameters (feedstocks, gas collection time, water injection rate and cyclic stability without regeneration) were investigated to optimize the H_2 production with the resultant mass balance, gas concentration shown in Table S2 and Fig. 1(a–d). TPO and derivative thermogravimetric temperature-programmed oxidation (DTG-TPO) indicate two types of carbon species can be distinguished based on their distinct oxidation peaks at different temperatures in Fig. 2(a–d). As clearly shown in the DTG-TPO curves, the peak slightly above 400 °C corresponds to the combustion of disordered/amorphous carbon, while the peak around 650 °C is attributed to the oxidation of graphitic/filamentous carbon [20,51].

By replacing PET with HDPE and LDPE as the feedstock, the H_2 yield increased significantly from 58.10 to 110.31 and 113.21 mmol g^{-1} $_{\text{of plastics}}$, respectively (Fig. 1a). This suggests that the hydrogen content in the feedstock plays a dominant role in determining H_2 production. According to the ultimate analysis (Table S1), PET contains 42.7 mg of H per gram of plastics. Using

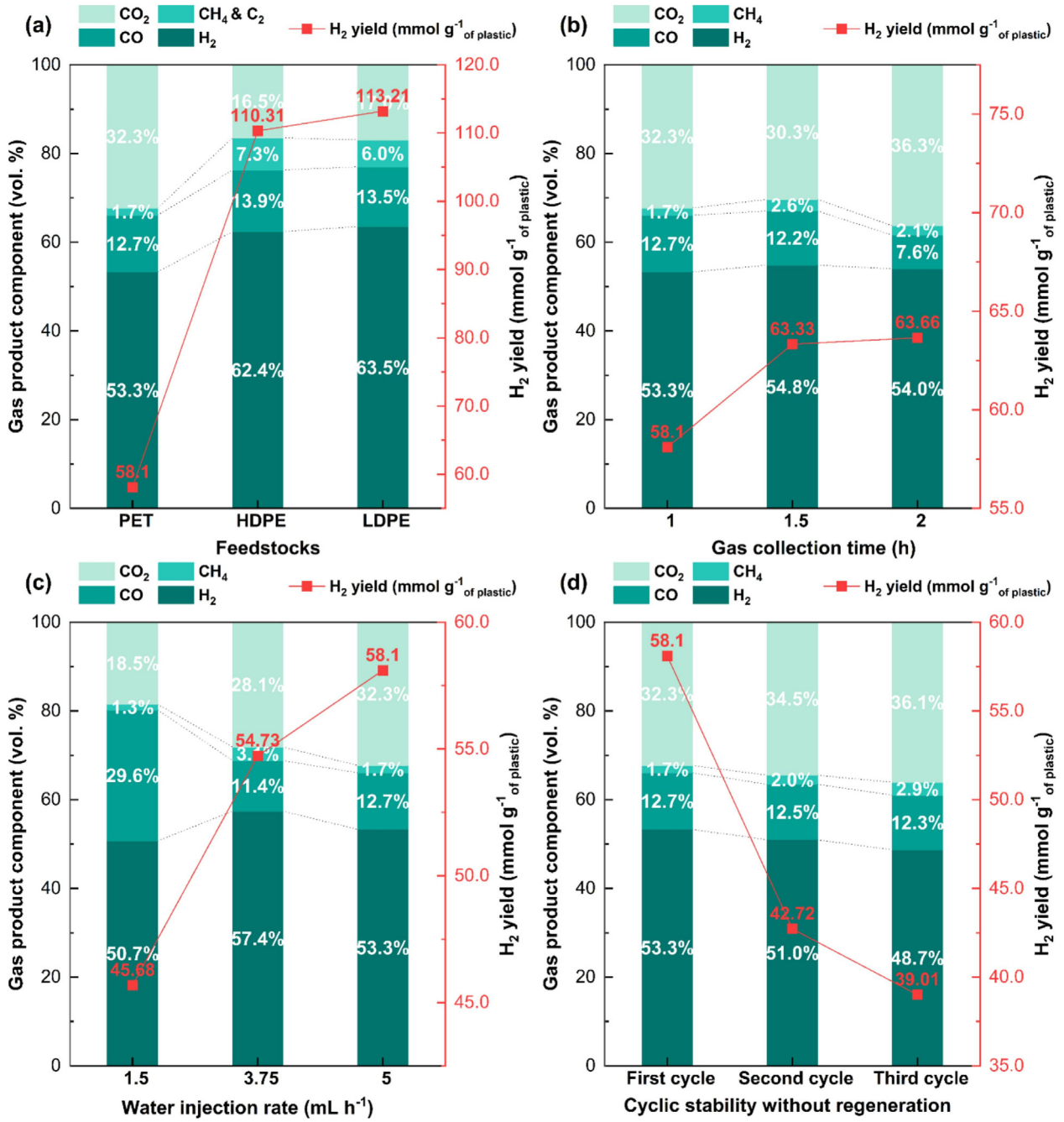

Fig. 1. Standard experimental conditions: PET as feedstock, N_2 flow rate of 110 mL min^{-1}, pyrolysis temperature of 600 °C and catalytic temperature of 900 °C. (a–d) Gaseous product yields from plastic waste pyrolysis–catalytic gasification process with different (a) feedstock, (b) gas collection time, (c) water injection rate, and (d) cyclic stability test of the catalyst without regeneration.

the same approach, HDPE and LDPE have H contents of 150.5 and 140.4 mg $g^{-1}_{of\ plastics}$. The approximate difference of ~100 mg $g^{-1}_{of\ plastics}$ between HDPE/LDPE and PET in H contents aligns well with the experimental results (110.31–58.1 mg $g^{-1}_{of\ plastics}$), reinforcing the strong correlation between feedstock H content and H_2 yield. This finding further confirms the involvement and significant contribution of water in H_2 production since PET feedstock contains only 21.35 mmol of H_2 g^{-1} $_{of\ plastic}$, while experimentally obtained H_2 yield reached 58 mmol g^{-1} $_{of\ plastic}$. Moreover, this does not account for hydrogen present in by-products such as methane (CH_4), as well as the minimal amounts of liquid fractions and coke. In Fig. 2(a), Tables S2 and S3, compared with PET, PE-based feedstocks resulted in higher carbon production, with carbon yields of 100.43 mg (1.74 wt%) and 118.24 mg (2.17 wt%) from HDPE and LDPE respectively, compared to 76.06 mg (1.39 wt%) from PET. This finding is consistent with the ultimate analysis research as shown in Table S1, where the C contents of HDPE and LDPE are around 86.22% and 81.83% respectively, compared with 62.78% for PET. Despite the increased coke formation, gas production remained promising, as indicated by the comparable or even higher H_2 yields. Notably, LDPE generated not only a larger quantity of carbon than HDPE but also a higher proportion of graphitic/filamentous carbon as shown in Fig. 2(a) and Table S3, which could be attributed to the higher yield of unsaturated or aromatic intermediates from LDPE pyrolysis, as these are prone to polycondensation and reorganization into more ordered carbonaceous structures over the Ni-based cata-

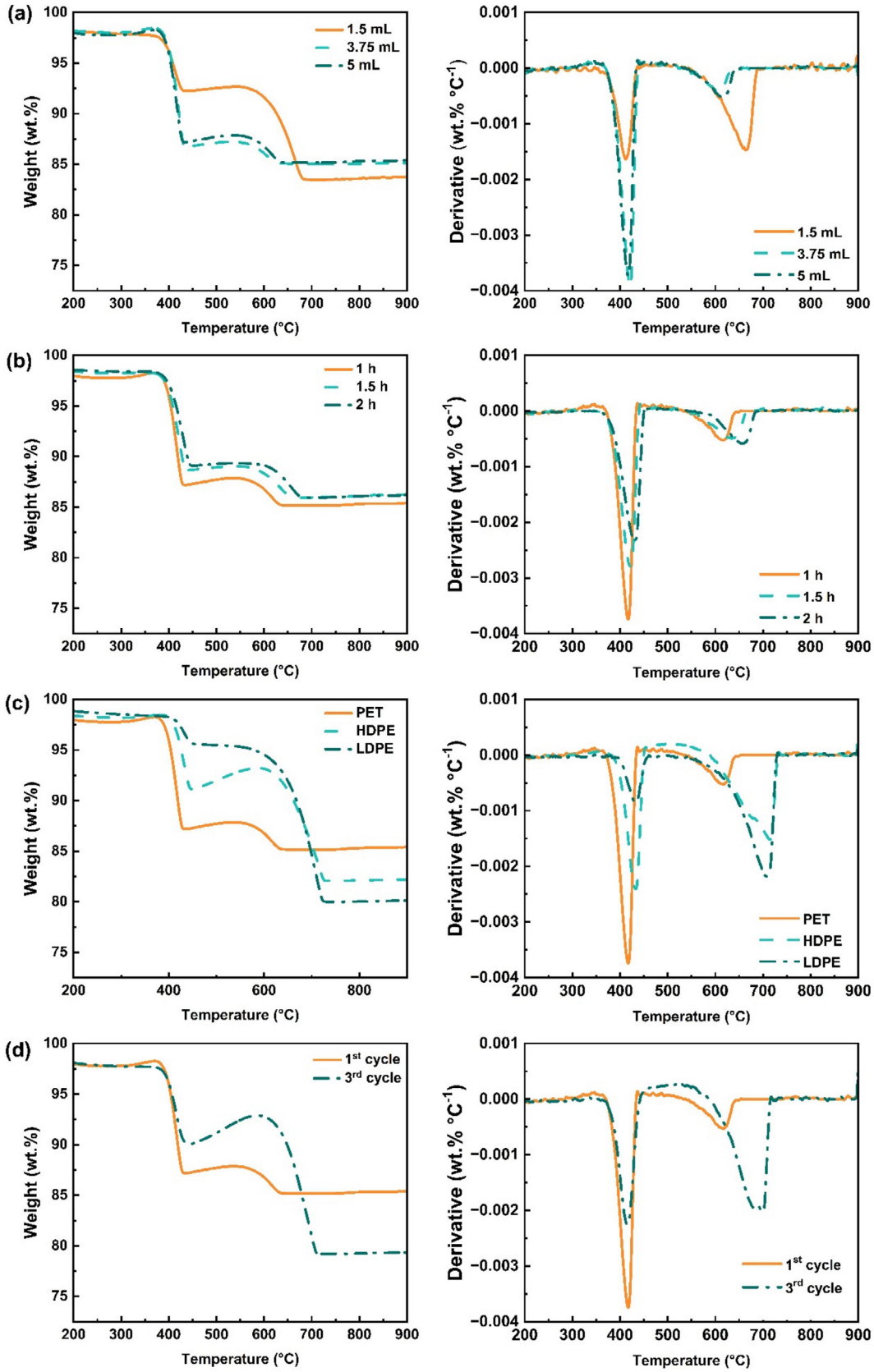

Fig. 2. (a–d) TPO and corresponding DTG-TPO results of spent catalysts with different (a) feedstock, (b) gas collection time, (c) water injection rate, and (d) cyclic stability test of the catalyst without regeneration.

lyst [52–54]. After approximately 30 min of gas collection, the feedstock is considered to have undergone complete pyrolysis. An additional 30 min is allocated to ensure the complete gasification and collection of all gaseous products.

To investigate the effect of extended reaction time on H_2 yield, the gas collection duration was prolonged to 1.5 and 2 h while maintaining the catalytic temperature at 900 °C, continuously supplying water without introducing additional feedstock (Fig. 1b). The results showed that extending collection period to 1.5 h resulted in an enhanced H_2 yield from 58.1 to 63.33 mmol $g^{-1}_{\text{of plastic}}$, with negligible further increase observed at 2 h (63.66 mmol $g^{-1}_{\text{of plastic}}$). Additionally, a slight decrease in carbon deposition was observed, mainly for amorphous carbon, as shown in Fig. 2(b) and Table S3. This suggests that the additional steam facilitated further reactions of coke and produced H_2 (Reaction (1) and Reaction (3). The similar amounts of coke deposits observed in TGA-TPO analyses for both 1.5-h and 2-h collections (Fig. 2b) indicate that all coke susceptible to the Reaction (1) and Reaction (3) had been consumed by 1.5 h. To investigate the effect of excess water on H_2 production, water injection rates were systematically varied at 1.5-, 3.75-, and 5-mL h^{-1} with gas collection time of 1 h (the stoichiometric amount of water required is 1.29 mL per gram of PE or 0.65 mL per gram of PET). The results indicate that excess water effectively shifted the reaction equilibrium to enhance H_2 production, with yields increasing from 45.68 to 54.73 then 58.1 mmol $g^{-1}_{\text{of plastic}}$ (Fig. 1c). Notably, syngas production initially decreased from 72.32 to 65.60 then 72.00 mmol $g^{-1}_{\text{of plastic}}$. This non-monotonic trend was accompanied by a significant increase in the CO_2 fraction in gaseous product at higher water injection rates, suggesting enhanced water–gas shift activity (Reaction (2).

According to the TPO data (Fig. 2c), a 1.5 mL h^{-1} of water injection rate resulted in a notably highest amount of carbon deposition of 4.26 wt% as shown in Table S2, particularly in the form of graphitic/filamentous carbon (Table S3). This observation suggests that an increase in water content can significantly alter not only the quantity but also the nature of the carbon formed. However, the TGA profiles for 3.5- and 5-mL h^{-1} of water injection rates were essentially identical, indicating that once an optimum amount of water is reached, further increasing the introduction of water no longer exerts a significant influence on the carbon deposition behavior. Additionally, an excessive amount of steam might lead to a more homogeneous gas-phase environment.

Cyclic stability tests were conducted without catalyst regeneration, and the H_2 yield decreased from 58.1 to 42.72 then 39.01 mmol $g^{-1}_{\text{of plastic}}$ from 1st to 3rd cycle of experiment (Fig. 1d). It is hypothesized that coke formed on the catalyst surface after the 1st cycle of experiment, blocking active sites and causing a significant decrease in H_2 yield in the 2nd cycle of experiment. Alongside H_2, syngas yield also decreased, while CO_2 and CH_4 production steadily increased. As further evidence, after 3rd consecutive catalytic cycles without regeneration, the weight of graphitic/filamentous carbon increased significantly from 15.76 to 78.47 mg (Fig. 2d and Table S3). This trend suggests that over multiple cycles, the catalyst surface becomes progressively covered with more stable, ordered carbon forms, which are less susceptible to gasification. The increase in ordered carbon supports the hypothesis that coke formation contributes to the reduction in H_2 production. Although the catalyst degraded significantly after three cycles, it still exhibited catalytic activity compared to the experiment without a catalyst in previous research [16], where H_2 production was only 37.46 mmol $g^{-1}_{\text{of plastic}}$. This finding further supports the potential of developing hybrid functional catalysts to enhance H_2 production from plastic waste pyrolysis–catalytic gasification process.

$$C + H_2O \rightleftharpoons CO + H_2 \quad (1)$$

$$CO + H_2O \rightleftharpoons CO_2 + H_2 \quad (2)$$

$$C + 2H_2 \rightleftharpoons CH_4 \quad (3)$$

$$CH_4 + H_2O \rightleftharpoons CO + 3H_2 \quad (4)$$

3.2. Pre- and post-reaction catalysts structural evolution

The SEM images of the spent catalysts after the 1st and 3rd cycles, with PET used as feedstock, are presented in Fig. 3(a–c) and Fig. 3(d–f), respectively. No significant differences in the overall surface morphology were observed, indicating that the catalyst maintained good structural stability after three cycles. To further investigate the distribution of active components, a specific region of spent catalyst following the 1st cycle was selected for SEM imaging (Fig. 3g) and EDS elemental mapping (Fig. 3h). In Fig. 3(h), blue color indicates the distribution of Ca, appearing uniformly distributed as the fundamental structural framework of the catalyst; yellow color indicates the distribution of Si while pink color indicates the distribution of Ni. As shown in Fig. 3(i), Ni particles were generally well-dispersed across the catalyst surface. It is worth noting that partial agglomeration of Ni particles was also observed in several areas, one of which is indicated by the red dashed circle. This phenomenon can be seen more clearly in Fig. 3(i).

As shown in Fig. 3(j), the fresh catalyst contains no detectable metallic Ni. It is primarily composed of NiO, with small amounts of $CaCO_3$ and a significant quantity of $Ca(OH)_2$. The presence of $Ca(OH)_2$ and $CaCO_3$ is likely a result of the hydration and carbonation of CaO upon exposure to atmospheric moisture and CO_2 during storage. After the 1st catalytic cycle, a notable amount of metallic Ni emerges, although traces of NiO remain detectable. This could be attributed to the continued presence of steam in the second stage of the reactor after the plastic has been fully decomposed from the first stage of the reactor, leading to partial re-oxidation of the previously reduced Ni species. Fig. 3(k) shows the XRD patterns of the spent catalysts after the 1st and 3rd cycles, while Fig. 3(l) provides a zoomed-in view of the 2θ range from 16° to 29°. A clear sharpening of the Ni diffraction peaks and further growth of the NiO phase are observed, suggesting that Ni sintering occurs during repeated reaction cycles.

The crystallite sizes of Ni and NiO, along with their molar ratio, were obtained through combined analysis using the Scherrer equation and Rietveld refinement [48,49] (Table S5). An investigation based on gas collection time revealed that the crystallite sizes of both Ni and NiO did not exhibit significant differences (Fig. 3m). However, the Ni/NiO molar ratio showed a pronounced decline (Fig. 3p). Decomposition of plastic sample was essentially completed within the first 30 min, yet water injection continued beyond this point. This sustained presence of steam after pyrolysis at elevated temperatures led to the gradual re-oxidation of the reduced Ni. Notably, by comparing gas collection times of 1 and 1.5 h, the Ni/NiO molar ratio had already dropped from 2.64 to around 0.88, indicating that the amount of NiO exceeded that of metallic Ni during this additional 30 min (Fig. 3p). After an additional 30 min to 2 h, this ratio decreased even further, reaching approximately 0.38, confirming the progressive Ni oxidation in the latter stage of the process.

Water plays a significant role in the catalytic pyrolysis-gasification process for H_2 production. Concurrently, by limiting the gas collection time to 1 h, the Ni/NiO molar ratio exhibited a notable rise from 0.88 to 1.66 and then to 2.64 as water injection rate increases (Fig. 3q). It is worth noting that even at 1.5 mL,

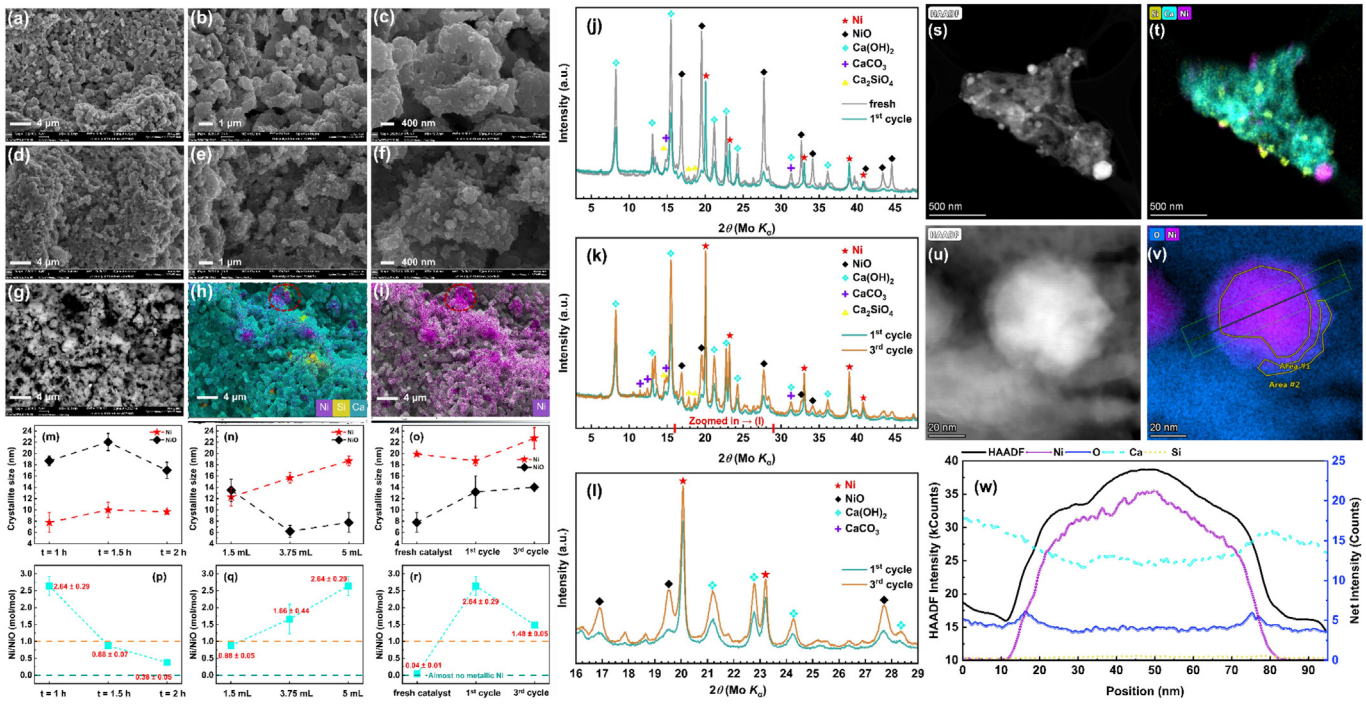

Fig. 3. SEM images of spent catalysts after the 1st cycle at different magnifications (a–c) and the 3rd cycle (d–f). (g) SEM image of a selected region of the catalyst after the 1st cycle and (h) corresponding EDS elemental mapping of the same region, showing the distribution of calcium (Ca), silicon (Si), and nickel (Ni). (i) EDS map of Ni. (j) Ex situ XRD patterns of fresh Ni-CaO-Ca_2SiO_4 and spent catalyst after the 1st cycle. (k) Ex situ XRD patterns of spent catalyst after the 1st and 3rd cycles. (l) Zoomed-in view of (k). (m–o) Crystallite sizes of Ni and NiO for spent catalysts. (p–r) Molar ratio of Ni/NiO for spent catalysts. (s–v) Representative HAADF-STEM images and EDS analysis of spent catalyst after the 1st cycle. (w) Line-scan profiles analysis of HAADF and EDS (O, Ni, Ca, and Si) intensities across the selected green region in (v).

the amount of water was already in excess under the given reaction conditions. Nevertheless, further increasing the water injection rate significantly enhanced the Ni/NiO molar ratio, which in turn improved the catalyst activity and boosted H_2 yield (Fig. 1c). Given that H_2 yield increases with water injection rate, these results suggest that water played a critical role in enhancing the gasification process of plastic. After the 1st and 3rd cycles, a slight increase in the crystallite sizes of Ni and NiO was observed in the spent catalysts (Fig. 3o) due to the sintering of Ni and NiO particles. After the 1st cycle, the Ni/NiO ratio increased significantly from 0.04 to 2.64, indicating the self-reduction of the catalyst during the reaction. After the 3rd cycle, the Ni/NiO molar ratio decreased from 2.64 to 1.48, which is believed to be one of the reasons for the catalyst's poor performance in H_2 production (Fig. 3r). HAADF-STEM imaging and EDS analysis were conducted on the spent catalyst after the first cycle to investigate the elemental distribution on the small catalyst particles (Fig. 3s–v). A representative Ni particle was selected to examine its oxidation behavior. EDS mapping (Fig. 3v) revealed that the oxygen intensity in the outer region of the Ni particle (area 2) was significantly higher than that in the inner region (area 1), indicating surface oxidation. This result was further supported by the EDS line-scan profiles acquired across the green-boxed region, as shown in Fig. 3(w). Notably, distinct peaks in the O intensity were observed at approximately 15 and 75 nm, corresponding to the oxidized outer layers of the Ni particle, while the inner region retained the structure of metallic Ni. This finding is consistent with the XRD results.

The surface elemental compositions of all samples were determined via XPS, with detailed results summarised in Table S4. Fig. 4(a–d) present the surface molar ratios of surface C/Ca for post-reaction catalysts obtained under varying reaction parameters. As calcium remains relatively stable during the reaction, this ratio is employed as an indicator of surface carbon enrichment. Higher surface C/Ca molar ratio values reflect greater surface carbon atomic percentages. In addition, the wt.% of carbonaceous deposition derived from TGA-TPO analyses are also included for comparison (Table S2).

Fig. 4(a) shows that using HDPE and LDPE as feedstocks results in more substantial coke on the catalyst surface than PET due to the higher C contents shown in Table S1. This observation aligns with the TGA-TPO results presented in Fig. 1(a) and Table S3. Extending reaction time to 2 h does not induce further carbon removal, as reflected by the minimal differences observed in both the surface C/Ca molar ratios and the C wt.% across the three samples (Fig. 4b). However, a closer inspection reveals that the surface Ni/Ca molar ratio increases moderately from 4.3% to 7.9% under prolonged reaction conditions (Fig. 4e). This observation suggests carbon removal during the reaction is unmasking the Ni on catalyst surface.

As shown in Fig. 4(c), increasing the water injection rate gradually reduces carbon deposition on catalyst surface, in agreement with earlier findings as shown in Fig. 2(c). Similarly, Fig. 4(d) confirms the accumulation of carbon over repeated catalytic cycles which is consistent with the TPO results as shown in Fig. 2(a). To further elucidate the nature of the deposited carbon species, XPS C 1*s* spectra of selected samples are presented in Fig. 4(f, g). A pronounced increase in the O–C=O peak at approximately 289.7 eV is observed, which may be partially attributed to the $CaCO_3$ (Fig. 3k) [28,55]. Fig. 4(h) presents the Ni 2*p* XPS spectra of the spent catalysts, providing further insight into the mechanisms of catalyst deactivation [16]. The XPS spectrum of the fresh catalyst can be found in our previous publication. Taking the 3rd cycle as an example, although XRD indicates the presence of metallic Ni, which in amount is approximately 1.48 times greater than that of NiO (Fig. 3r), XPS reveals that almost no metallic Ni^0 (Ni $2p_3/_2$ = 852.6 eV) is detected at the surface [56]. Considering the

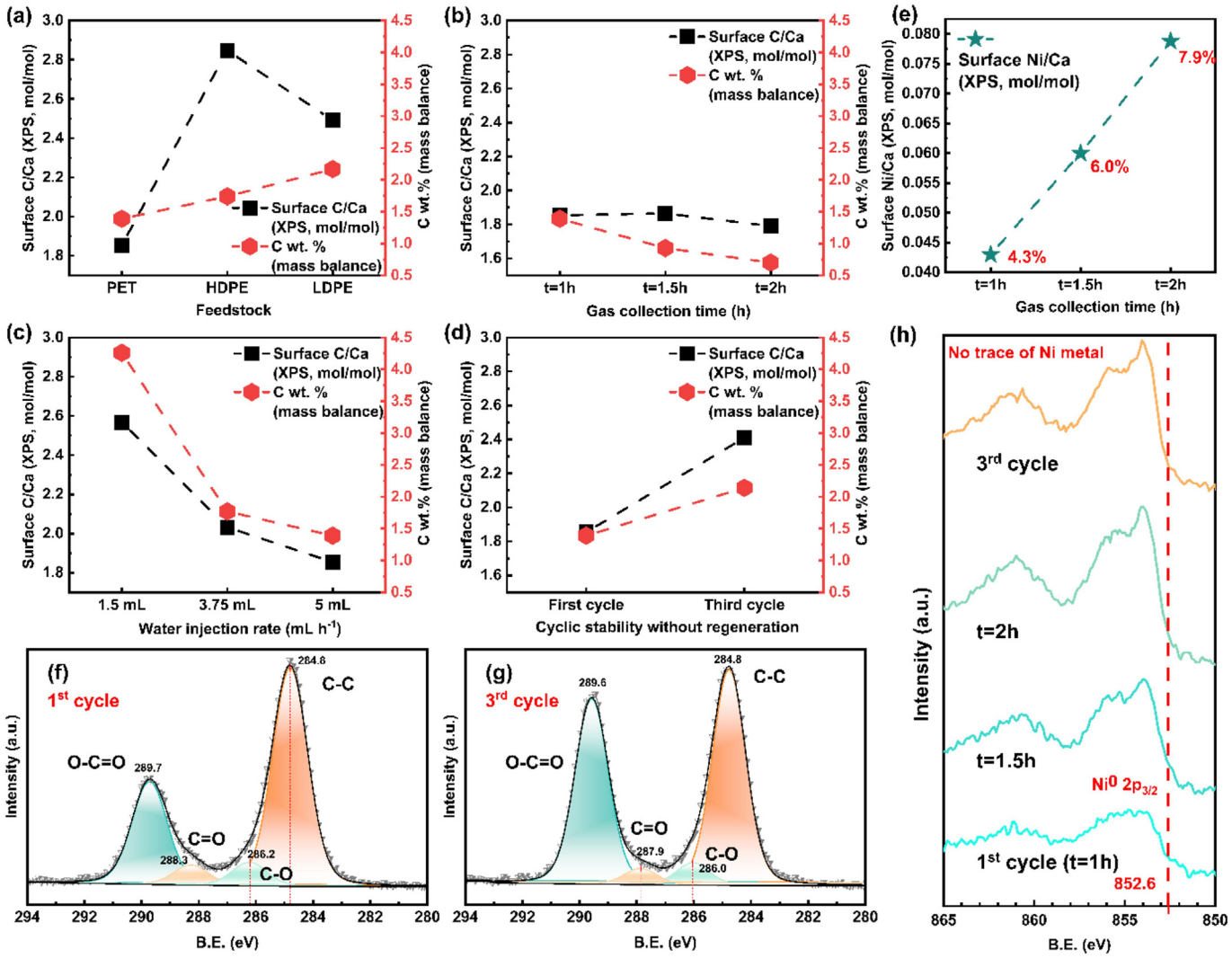

Fig. 4. Surface C/Ca molar ratio by XPS and carbon wt.% by mass balance for spent catalysts with relative parameters (a–d). (e) Surface Ni/Ca molar ratio by XPS for (b). (f, g) C 1*s* XPS spectra for spent catalysts after the 1st and 3rd cycles. (h) Ni 2*p* XPS spectra for spent catalysts.

surface-sensitive nature of XPS (a few nanometers in depth) and the bulk-penetrating ability of XRD and given that the surface atomic concentration of Ni remains low (<1.6%, see Table S4), it is inferred that the remaining active Ni species are predominantly confined within the porous structure of the catalyst, which is likely obstructed by accumulated carbon deposition, particularly after repeated use. This finding is consistent with previous reports, which demonstrated that catalyst deactivation predominantly occurs at or near the outer surface, where substantial pore blockage by accumulated coke restricts access to internal active sites [29,57]. As a result, the reduced accessibility of these Ni sites could account for the observed decline in catalytic activity.

3.3. In situ characterization and mechanistic insights

The performance optimization results and ex situ characterization discussed above suggest that catalyst deactivation is associated not only with coke accumulation, but also with the evolution of Ni-containing phases. Particularly, ex situ XRD of the spent catalyst revealed the oxidation of metallic Ni, accompanied by apparent Ni crystallite growth, suggesting that structural changes in the active phase may contribute to the observed deactivation behaviour. To further elucidate the progression of these phase transformations under reaction-relevant conditions, in situ PXRD was employed to monitor the oxidation/reduction behaviour and crystallite evolution of Ni-containing phases.

The evolution of PXRD diffraction data from fresh Ni-CaO-Ca_2SiO_4 catalyst during the heating from room temperature (RT) to 900 °C, followed by a 30-min isothermal stage at 900 °C (denoted as 900 °C*) is reported in Fig. 5(a). Upon heating from RT to 400 °C, the catalyst structure remained largely stable. In the 400–500 °C range, HDPE underwent thermal decomposition (Fig. S2), generating reductive gases that led to the emergence of metallic Ni peaks, providing clear evidence of NiO reduction. This in situ reduction marked the onset of catalytic activity, likely facilitating further cracking of the pyrolysis volatiles. Upon increasing the temperature to 500–600 °C, $Ca(OH)_2$ vanished entirely, as evidenced by pronounced reflections corresponding to both CaO and $CaCO_3$. The $CaCO_3$ phase showed significant growth between 400 and 500 °C, after which it nearly disappeared by 700 °C, indicating near-complete decomposition.

Given the absence of oxygen in both the PE feedstock and the N_2 carrier gas, the formation of $CaCO_3$ implies that the oxygen source might be the reduction product of NiO, or water released during Ca $(OH)_2$ decomposition [58,59]. The latter could have reacted with pyrolysis gases to generate CO_2, which was subsequently captured by CaO. This low-temperature structural transformation warrants further investigation to understand the mechanism of transforma-

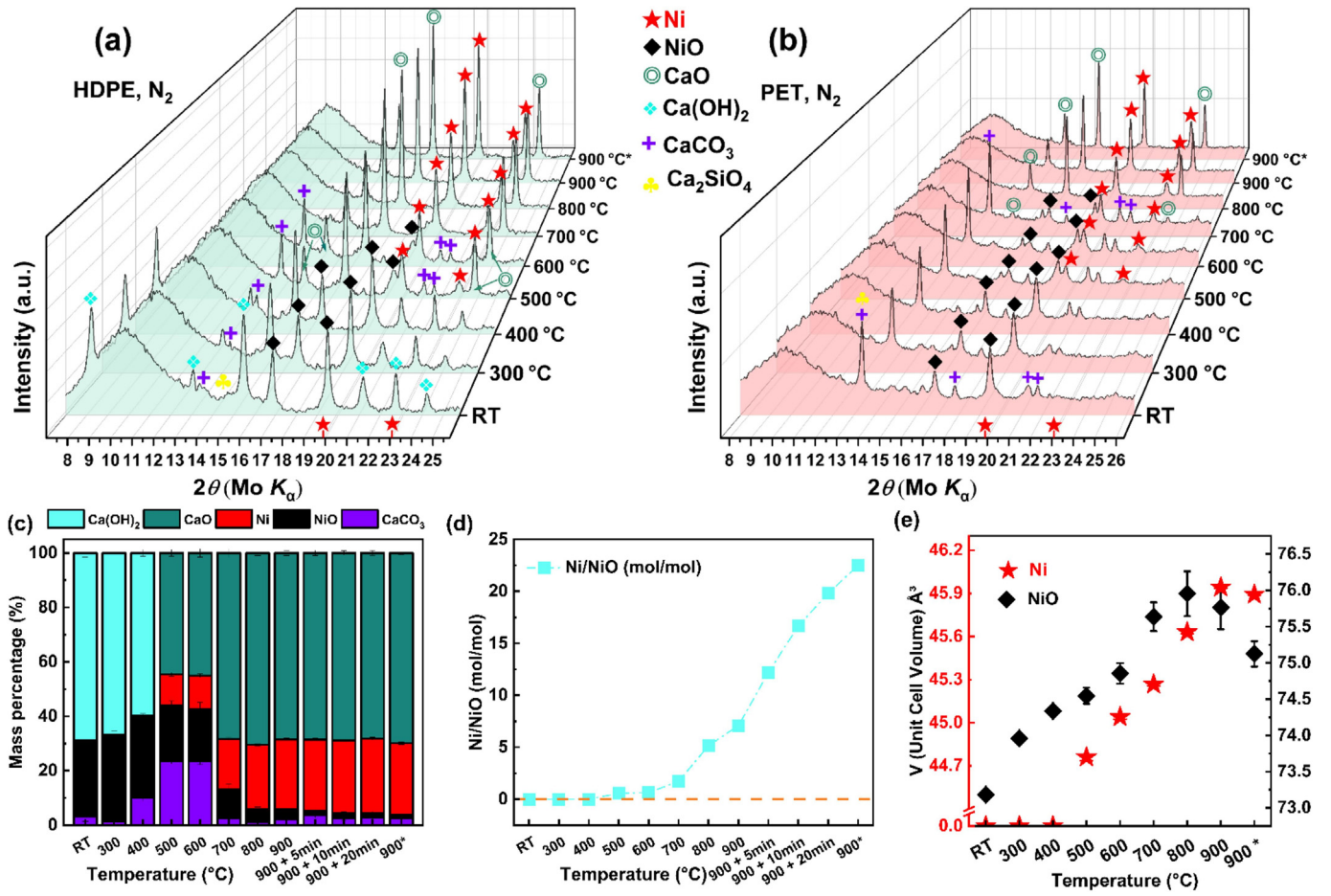

Fig. 5. In situ PXRD patterns of Ni-CaO-Ca_2SiO_4 were recorded at a ramping rate of 50 °C min^{-1}, with 2.5 min scans at every 100 °C, and continuous scanning every 2.5 min after 900 °C (900 °C* refers to the isothermal stage at 900 °C for 30 min). (a) HDPE. (b) PET. (c) Calculated mass percentage evolution in the catalyst shown in (a). (d) Evolution of Ni/NiO molar ratio of catalyst in (a). (e) Unit cell volume evolution of Ni and NiO of catalyst in (a).

tions between $Ca(OH)_2$, CaO, and $CaCO_3$ in the presence of gases released during thermal decomposition of plastic. While CaO is likely to be a decomposition product of $Ca(OH)_2$, $CaCO_3$ is likely to be formed from CaO via fast absorption of CO_2 gas; but $CaCO_3$ is not thermodynamically stable at high temperatures thus it further decomposes into CaO with release of CO_2 gas which partially re-oxidizes the metallic Ni to NiO. At higher temperatures (above 700 °C), the catalyst structure stabilized, with only Ni and CaO phases dominating.

Residual NiO was minimal and progressively reduced with increasing temperature (Fig. 5d), likely due to the diffusion of the remaining pyrolysis gases in the quartz capillary during the heating process, even after HDPE decomposition had concluded. Additionally, as shown in Fig. 5(e) and Table S6, the progressive formation of metallic Ni was observed from 500 °C (the diffraction data at previous temperature step 400 °C indicated no Ni in the sample) and the unit cell volume of Ni gradually increased with temperature due to thermal expansion. The unit cell volume of NiO also exhibited thermal expansion with increasing temperature. In situ XRD analysis was also conducted with PET-loaded samples (Fig. 5b). Only strong reflections from $CaCO_3$ and NiO were observed at RT, whereas $Ca(OH)_2$ was absent, possibly due to differences in storage conditions. Given that PET pyrolyzes between 400 and 500 °C (Fig. S2), the appearance of metallic Ni and the concurrent attenuation of NiO reflections at 500 °C are consistent with its thermal behavior. Notably, in contrast to HDPE-loaded sample, in which CaO was already detectable at 500 °C (Fig. 5a), only a weak CaO reflection was observed at 700 °C in PET-loaded sample, together with $CaCO_3$ (Fig. 5b). Eventually, both NiO and $CaCO_3$ were no longer detectable within the observable scale, and the sample remained stable thereafter.

The in situ PXRD data for the PET-loaded sample are presented on the Fig. 6(a). The main difference compared to Fig. 5(b) is the slower heating rate, with scans taken every 5 °C and a 2.5-min hold at each temperature, ramp rate between temperature points is 50 °C. Fig. 6(d) provides a clear indication of the processes occurring during step heating by listing the mass percentages of each component. Prior to the onset of PET pyrolysis, $Ca(OH)_2$ decomposes at approximately 400 °C, producing a small amount of CaO. This process proceeds only until around 430 °C, beyond which CaO begins to absorb CO_2, resulting in the formation of thermodynamically stable $CaCO_3$. Notably, no coexistence of Ni and CaO are observed until all available CaO has been consumed, suggesting that under these conditions, the pyrolysis gases from PET are preferentially captured by CaO rather than acting as reducing agents for NiO. Given the extended reaction and scan duration, it can be reasonably assumed that only minimal pyrolysis gas remains by approximately 640 °C.

Interestingly, a sharp decline in the wt.% of Ni is observed between 640 and 680 °C, after which the crystalline composition is dominated by CaO and NiO. This observation is further supported by the molar ratio of Ni/NiO shown in Fig. S3 and Table S7. We propose that this abrupt transformation is attributable to the decomposition of $CaCO_3$ at slow heating within this tem-

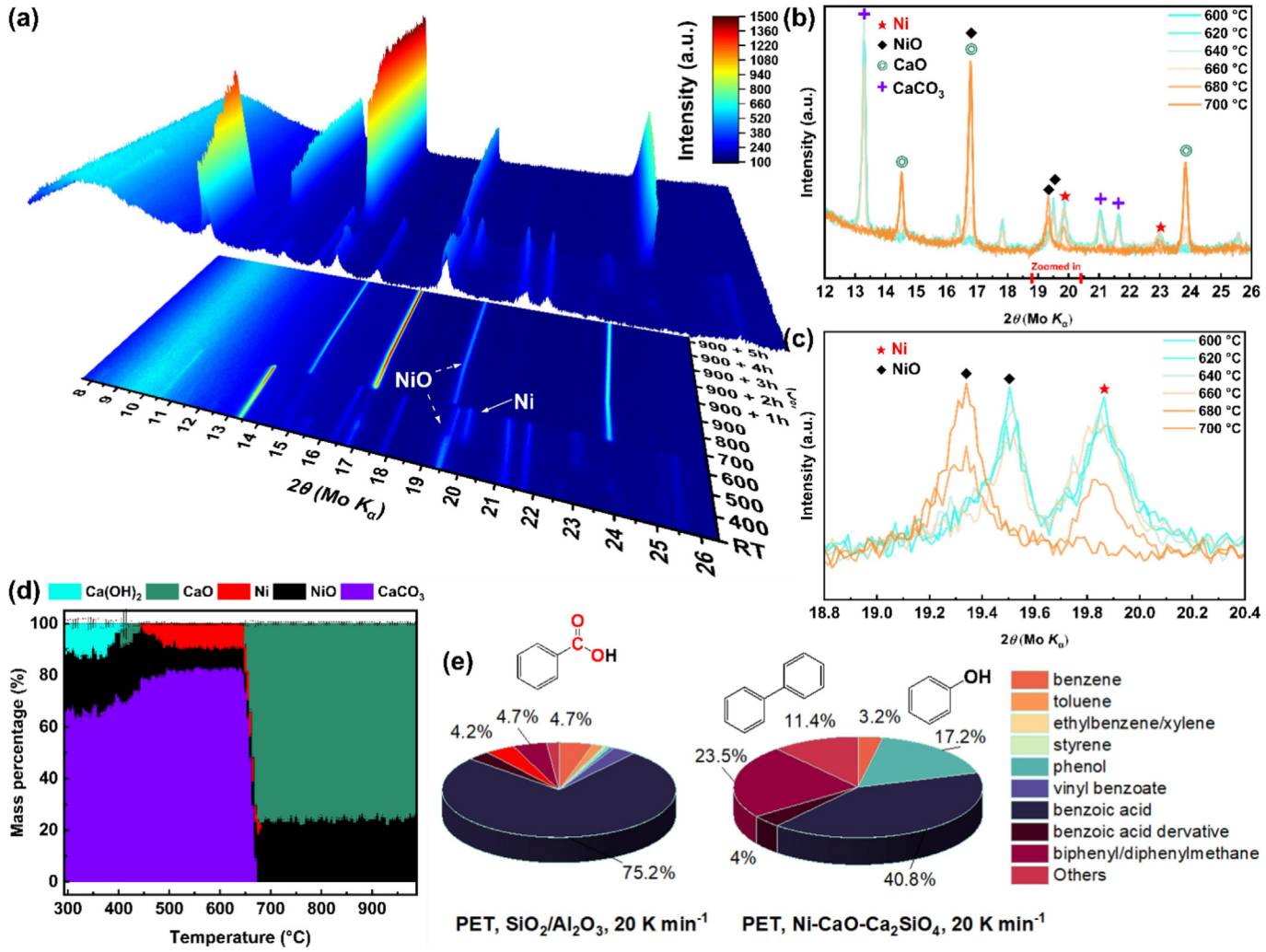

Fig. 6. (a, b) In situ PXRD patterns of Ni-CaO-Ca_2SiO_4, PET loaded, N_2 flow, 20 °C min^{-1} ramping rate, with scans every 5 °C, hold at 900 °C for 6 h with scans every 2.5 min. (c) zoomed-in view of (b) to demonstrate the reduction of NiO. (d) Calculated mass evolution of catalyst in (a). (e) Distribution of pyrolysis products collected from for the experiments conducted by a Py-GCMS with PET mixed with SiO_2/Al_2O_3 and Ni-CaO-Ca_2SiO_4, respectively.

perature range, which leads to the release of a significant amount of CO_2, thereby oxidizing Ni to NiO. The detailed structural evolution of the sample between 600 and 700 °C within a specific 2θ range of diffraction data is shown in Fig. 6(b), while Fig. 6(c) presents a zoomed-in view of the same region. It reveals a progressive reduction in the intensity of the Ni peak, which ultimately disappears within the 680–700 °C range. Simultaneously, a slight shift in the NiO peak is observed due to thermal expansion (Fig. 6a–c). Such peak shifts are reversible, with the NiO peak position returning to its original state upon cooling to RT (Fig. S4). After reaching 680 °C, no detectable trace of metallic Ni remains. In addition, a pyrolysis-catalysis product analysis was conducted with the designed hybrid functional catalyst (Fig. 6e). The left-hand pie chart represents the sample comprising only SiO_2/Al_2O_3 without any metal loading as the blank experiment. Compared with the former, the Ni-CaO-Ca_2SiO_4 catalyst significantly suppressed the formation of benzoic acid, while facilitating the production of biphenyl and other non-carboxylate aromatic derivatives [40,60]. This shift in product selectivity is primarily ascribed to the CO_2 adsorption capability of CaO. Nevertheless, under the high reaction temperature of 900 °C, the captured CO_2 is rapidly released, thereby shifting the reaction equilibrium and favoring the generation of deoxygenated products.

The key contribution of the in situ PXRD analysis is therefore to determine when and how the Ni/NiO transformation and Ca-containing phase evolution occur during the reaction process. By directly tracking these dynamic structural changes, the analysis links catalyst activation, Ni re-oxidation, and phase evolution to the deactivation behaviour identified by ex situ characterization, providing mechanistic information beyond post-reaction analysis alone.

4. Conclusions

In this study, hybrid-functional Ni-CaO-Ca_2SiO_4 catalyst was prepared and investigated for pyrolysis–catalytic gasification of plastic waste, achieving the highest H_2 yield of 113.21 mmol $g^{-1}_{\text{of plastic}}$ with LDPE as feedstock. Increasing water injection rate not only enhanced the yield of H_2 but also improved catalyst activity, as indicated by higher Ni/NiO ratio. After three reaction cycles, slight sintering of Ni particles was observed, accompanied by a reduction in the overall metallic Ni content within the catalyst and significant accumulation of inorganic O–C=O species. This finding is proven by the detection of oxidized shell formation on the outer surface of metallic Ni particles, while XPS revealed that only NiO was present on the catalyst surface, suggesting that deactiva-

tion initiates from the outermost regions. These findings suggest that avoiding Ni oxidation at the outer particle surface may help mitigate catalyst deactivation in future designs. The in situ PXRD patterns demonstrated the reduction of NiO to metallic Ni by pyrolysis products derived from plastic decomposition. The above findings provide meaningful insights into the rational design of advanced catalysts with enhanced stability, activity, and resistance to deactivation under realistic, cyclic operating conditions. Moreover, this study proposes an approach that employs in situ and ex situ PXRD data to analyze catalyst crystal structures, integrated with SEM, STEM and XPS characterization as well as catalytic performance results, providing a valuable reference for future novel catalyst investigations and supports the global 'Net Zero' ambition.

CRediT authorship contribution statement

Tian Heng Qin: Writing – original draft, Methodology, Investigation, Formal analysis. **Oxana V. Magdysyuk:** Writing – review & editing, Investigation, Funding acquisition, Formal analysis, Data curation. **Shaoliang Guan:** Writing – review & editing, Funding acquisition, Formal analysis, Data curation. **Zhuze Shao:** Writing – review & editing, Investigation. **Tian Wang:** Writing – review & editing. **Shogo Kumagai:** Writing – review & editing, Resources. **Toshiaki Yoshioka:** Writing – review & editing, Resources. **Boyu Qu:** Writing – review & editing, Resources. **Guozhao Ji:** Writing – review & editing, Validation, Methodology, Funding acquisition. **Davide Dionisi:** Writing – review & editing, Resources. **Jos Derksen:** Writing – review & editing, Supervision. **Ye Shui Zhang:** Writing – review & editing, Validation, Supervision, Resources, Project administration, Methodology, Investigation, Funding acquisition, Formal analysis, Conceptualization.

Declaration of competing interest

The authors declare the following financial interests/personal relationships which may be considered as potential competing interests: Ye Shui Zhang reports financial support, administrative support, article publishing charges, and equipment, drugs, or supplies were provided by University of Aberdeen. Oxana V. Magdysyuk reports financial support, administrative support, and equipment, drugs, or supplies were provided by University of St Andrews. Shaoliang Guan reports financial support, administrative support, and equipment, drugs, or supplies were provided by University of Cambridge. Toshiaki Yoshioka reports administrative support and equipment, drugs, or supplies were provided by Tohoku University. Guozhao Ji reports administrative support and equipment, drugs, or supplies were provided by Dalian University of Technology. If there are other authors, they declare that they have no known competing financial interests or personal relationships that could have appeared to influence the work reported in this paper.

Acknowledgements

Co-funded by the European Union (HyWay:101130009). Views and opinions expressed are however those of the author(s) only and do not necessarily reflect those of the European Union or the Research Executive Agency. Neither the European Union nor the Research Executive Agency can be held responsible for them.

This work was funded by UK Research and Innovation (UKRI) under the UK government's Horizon Europe funding guarantee [EP/Y036751/1] as well as the National Key Research and Development Program of China (2025YFE0109700).

This work was supported by the Henry Royce Institute for advanced materials through the Equipment Access Scheme enabling access to the XPS at Cambridge; (Cambridge Royce facilities grant EP/P024947/1 and Sir Henry Royce Institute - recurrent grant EP/R00661X/1). This work was also supported by the Scotland Beyond 'Net Zero' Seed Funding (3871389). Authors acknowledge the support from EPSRC Core Equipment Grant (EP/V034138/1) for powder diffractometers.

Appendix A. Supplementary material

Supplementary data to this article can be found online at https://doi.org/10.1016/j.jechem.2026.07.030.

References

[1] L. Europe, Plastics – the Fast Facts 2024, Plastics Europe, Brussels, 2024.
[2] M. Bergmann, B.C. Almroth, S.M. Brander, T. Dey, D.S. Green, S. Gundogdu, A. Krieger, M. Wagner, T.R. Walker, Science 376 (2022) 469–470.
[3] International Energy Agency (IEA), Global Hydrogen Review 2024, IEA, Paris, 2024.
[4] International Energy Agency (IEA), The Future of Hydrogen: Seizing Today's Opportunities, Report prepared for the G20, IEA, Paris, 2019.
[5] M. Gao, J. Fan, X. Li, Q. Wang, D. Li, J. Feng, X. Duan, Angew. Chem. 135 (2023) e202216527.
[6] T.K. Anh Nguyen, T. Tr n-Phú, R. Daiyan, X. Minh Chau Ta, R. Amal, A. Tricoli,, Angew. Chem. Int. Ed. 63 (2024) e202401746.
[7] Q. Liu, S. Du, T. Liu, L. Gong, Y. Wu, J. Lin, P. Yang, G. Huang, M. Li, Y. Wu, Angew. Chem. 136 (2024) e202315157.
[8] H. Zhang, Y. Wang, X. Li, K. Deng, H. Yu, Y. Xu, H. Wang, Z. Wang, L. Wang, Appl. Catal. B Environ. 340 (2024) 123236.
[9] X. Yu, Z. Rao, G. Chen, Y. Yang, S. Yoon, L. Liu, Z. Huang, M. Widenmeyer, H. Guo, G. Homm, Angew. Chem. Int. Ed. 63 (2024) e202404196.
[10] G. Chen, X. Tu, G. Homm, A. Weidenkaff, Nat. Rev. Mater. 7 (2022) 333–334.
[11] R. Gu, T. Wang, Y. Ma, T.X. Wang, R.Q. Yao, Y. Zhao, Z. Wen, G.F. Han, X.Y. Lang, Q. Jiang, Angew. Chem. Int. Ed. 64 (2025) e202417644.
[12] S. Sun, Y. Wang, Y. Xu, H. Sun, X. Zhao, Y. Zhang, X. Yang, X. Bie, M. Wu, C. Zhang, Appl. Catal. B Environ. Energy 348 (2024) 123838.
[13] J. Zou, L. Zhao, Q. Hu, D. Yao, H. Yang, Appl. Energy 362 (2024) 122844.
[14] L. Chen, Z. Song, S. Zhang, C.-K. Chang, Y.-C. Chuang, X. Peng, C. Dun, J.J. Urban, J. Guo, J.-L. Chen, Science 381 (2023) 857–861.
[15] L. Jurado, V. Papaefthimiou, S. Thomas, A.-C. Roger, Appl. Catal. B Environ. 299 (2021) 120687.
[16] T.H. Qin, G. Ji, B. Qu, A.J. McCue, S. Guan, J. Derksen, Y.S. Zhang, Carbon Capture Sci. Technol. 14 (2025) 100382.
[17] D. Yao, Y. Zhang, P.T. Williams, H. Yang, H. Chen, Appl. Catal. B Environ. 221 (2018) 584–597.
[18] C. Wu, P.T. Williams, Appl. Catal. B Environ. 87 (2009) 152–161.
[19] C. Wu, P.T. Williams, Fuel 89 (2010) 3022–3032.
[20] C. Wu, P.T. Williams, Appl. Catal. B Environ. 96 (2010) 198–207.
[21] Y. Zhang, J. Huang, P.T. Williams, Energy Fuels 31 (2017) 8497–8504.
[22] R. Tu, J. Sun, Y. Xu, H. Yang, X. Fang, L. Zhang, J. Yang, G. Ren, X. Ci, W. Deng, Appl. Catal. B Environ. Energy 353 (2024) 124085.
[23] X. Cao, S. Wu, J. Zhao, F. Long, S. Jia, X. Zhang, J. Xu, J. Jiang, Appl. Catal. B Environ. 343 (2024) 123506.
[24] Q. Shang, D. Feng, X. Zhang, Z. Cheng, S. Wang, Y. Zhao, S. Sun, Appl. Catal. B Environ. Energy 379 (2025) 125695.
[25] L. Briones, A. Cordero, M. Alonso-Doncel, D. Serrano, J. Escola, Appl. Catal. B Environ. 341 (2024) 123359.
[26] Y. Zhang, S. Li, Y. Fu, L. Zheng, H. Li, W. Kong, B. Pan, J. Li, J. Zhang, Y. Sun, Appl. Catal. B Environ. Energy 350 (2024) 123903.
[27] Y.S. Zhang, H.L. Zhu, D. Yao, P.T. Williams, C. Wu, D. Xu, Q. Hu, G. Manos, L. Yu, M. Zhao, Sustain. Energy Fuels 5 (2021) 4173–4208.
[28] Q. Wu, L. Ke, Y. Wang, N. Zhou, H. Li, Q. Yang, J. Xu, L. Dai, R. Zou, Y. Liu, Appl. Catal. B Environ. 304 (2022) 120968.
[29] Y.S. Zhang, X. Lu, R.E. Owen, G. Manos, R. Xu, F.R. Wang, W.C. Maskell, P.R. Shearing, D.J. Brett, Appl. Catal. B Environ. 263 (2020) 118329.
[30] H. Zhou, J.M. Saad, Q. Li, Y. Xu, Waste Manag. 104 (2020) 42–50.
[31] Y. Li, M.A. Nahil, P.T. Williams, Chem. Eng. J. 467 (2023) 143427.
[32] G. Ji, X. Xu, H. Yang, X. Zhao, X. He, M. Zhao, Environ. Sci. Technol. 51 (2017) 11484–11492.
[33] X. Hu, D. Xu, J. Jiang, Angew. Chem. 137 (2025) e202419103.
[34] Y. Zhu, J. Miao, Y. Wang, D. Liu, Y. Zhang, X. Zhao, J. Hu, C. Wu, Chem. Eng. J. 484 (2024) 149778.
[35] S. Kumagai, Y. Morohoshi, G. Grause, T. Kameda, T. Yoshioka, RSC Adv. 5 (2015) (1837) 61828–61837.
[36] Y. Wang, H. Zhou, D. Yao, G. Olguin, H. Ding, B. Qu, W. Xie, Z. Fu, Y. Guo, X. Wang, J. Clean. Prod. 446 (2024) 141397.
[37] C.J. Wrasman, A.N. Wilson, O.D. Mante, K. Iisa, A. Dutta, M.S. Talmadge, D.C. Dayton, S. Uppili, M.J. Watson, X. Xu, Nat. Catal. 6 (2023) 563–573.
[38] X. Si, R. Lu, Z. Zhao, X. Yang, F. Wang, H. Jiang, X. Luo, A. Wang, Z. Feng, J. Xu, Nat. Commun. 13 (2022) 258.

[39] Y. Wang, M.Z. Memon, Q. Xie, Y. Gao, A. Li, W. Fu, Z. Wu, Y. Dong, G. Ji, Carbon Capture Sci. Technol. 2 (2022) 100033.
[40] Q. Chen, F. Xu, P. Zong, F. Song, B. Wang, Y. Tian, F. Wu, X. Zhao, Y. Qiao, J. Hazard. Mater. 436 (2022) 129220.
[41] S. Sun, C. Zhang, Y. Wang, X. Zhao, H. Sun, C. Wu, Chem. Eng. J. 468 (2023) 143712.
[42] A. Zhang, D. Li, X. Zhu, G.-M. Kim, Y. Zeng, C.-H. Jeon, H. Wang, T. Zhu, G. Bao, Energy Convers. Manag. 332 (2025) 119735.
[43] B. Zhang, Q. Lu, W. Huang, Y. Chen, W. Yan, B. Yu, X. Yang, J. Zhang, Int. J. Hydrogen Energy 47 (2022) 6605–6619.
[44] M. Wu, S. Zhang, S. Sun, Y. Yang, D. Yao, G. Ji, Y. Zhang, Q. Li, Y. Zhang, X. Bie, Sep. Purif. Technol. 379 (2025) 134769.
[45] C.F.M. Mbeugang, B. Li, D. Lin, X. Xie, S. Wang, S. Wang, S. Zhang, Y. Huang, D. Liu, Q. Wang, Energy 228 (2021) 120659.
[46] M. Bakhtiar, M. Shahbaz, H.M.U. Ayub, U. Ali, Energy 334 (2025) 137718.
[47] P. Zhang, C. Liang, M. Wu, Y. Li, X. Chen, D. Liu, J. Ma, Appl. Catal. B Environ. Energy 345 (2024) 123718.
[48] H. Rietveld, Acta Crystallogr. 22 (1967) 151–152.
[49] H.M. Rietveld, J. Appl. Crystallogr. 2 (1969) 65–71.
[50] A.A. Coelho, J. Appl. Crystallogr. 51 (2018) 210–218.
[51] Y. Zhang, C. Wu, M.A. Nahil, P. Williams, Energy Fuels 29 (2015) 3328–3334.
[52] P.T. Williams, Waste Biomass Valorization 12 (2021) 1–28.
[53] Z. Zhang, H. Chen, G. Li, W. Hu, B. Niu, D. Long, Y. Zhang, ACS Catal. 14 (2024) 2552–2561.
[54] X. Tian, Y. Wang, Z. Zeng, L. Dai, J. Xu, K. Cobb, L. Ke, R. Zou, Y. Liu, R. Ruan, Green Chem. 24 (2022) 3922–3942.
[55] Y. Zhang, Z. Fu, W. Wang, G. Ji, M. Zhao, A. Li, A.C.S. Sustain, Chem. Eng. 10 (2021) 91–103.
[56] A.P. Grosvenor, M.C. Biesinger, R.S.C. Smart, N.S. McIntyre, Surf. Sci. 600 (2006) 1771–1779.
[57] D. Xu, X. Lu, Y. Zhang, P.R. Shearing, S. Zhang, D.J. Brett, S. Wang, Chem. Eng. J. 450 (2022) 138402.
[58] C. Vogt;, M. Monai, E.B. Sterk, J. Palle, A.E. Melcherts, B. Zijlstra, E. Groeneveld, P.H. Berben, J.M. Boereboom, E.J. Hensen, Nat. Commun. 10 (2019) 5330.
[59] Y. Wang, Y. Li, G. Wang, J. Zhu, H. Yang, L. Jin, S. Hu, H. Hu, Fuel 324 (2022) 124742.
[60] S. Kumagai, G. Grause, T. Kameda, T. Takano, H. Horiuchi, T. Yoshioka, Ind. Eng. Chem. Res. 50 (2011) 1831–1836.

Tianheng Qin is a PhD candidate in Chemical Engineering at the University of Aberdeen, UK. He received his MSc degree in Chemistry from the University of Manchester and his BSc degree from the University of Reading. His research focuses on catalytic thermochemical conversion of waste plastics into hydrogen-rich syngas, with particular emphasis on Ni-based catalysts, catalyst deactivation and in-situ/operando characterisation. His current work aims to understand catalyst structural evolution under reaction conditions and to develop efficient catalytic processes for sustainable hydrogen production from waste solid.

Yeshui Zhang is a Lecturer in Chemical Engineering in the School of Engineering at the University of Aberdeen, UK. Previously, she was a Faraday Institution Research Fellow at University College London, UK. She holds a BSc from the University of Birmingham, an MSc (Engineering) from the University of Sheffield, and a PhD from the University of Leeds. Her research interests span a broad range of topics in chemical engineering, including energy storage materials, lithium-ion battery manufacturing, waste pyrolysis and catalytic conversion, high-temperature quartz crystal microbalance techniques, carbon capture technologies, carbon nanotube synthesis, and the circular economy of plastics.